JOURNAL OF MAGNETIC RESONANCE IMAGING 26:498–509 (2007)

**Original Research**

# Whole-Body MR Imaging vs. FDG-PET: Comparison of Accuracy of M-Stage Diagnosis for Lung Cancer Patients

Yoshiharu Ohno, MD, PhD,[1]* Hisanobu Koyama, MD,[1] Munenobu Nogami, MD,[1] Daisuke Takenaka, MD,[1] Takeshi Yoshikawa, MD,[1] Masahiro Yoshimura, MD,[2] Yoshikazu Kotani, MD,[3] Yoshihiro Nishimura, MD,[3] Takanori Higashino, MD,[1,4] and Kazuro Sugimura, MD[1]

**Purpose:** To conduct a prospective comparison of the accuracy of whole-body MR imaging and positron emission tomography (PET) with fluorine-18 deoxyglucose (FDG) (FDG-PET) to assess the M-stage in lung cancer patients.

**Materials and Methods:** A total of 90 consecutive lung cancer patients (mean age = 68 years) underwent whole-body MR imaging and FDG-PET as well as other standard radiological imaging procedures before and after treatment. Probabilities of metastases on whole-body MR imaging and FDG-PET were assessed by using 5-point scoring systems on a per-site basis and on a per-patient basis. Receiver operating characteristic (ROC) curve analysis was used to compare diagnostic capabilities. Sensitivity, specificity, and accuracy were also compared by using the McNemar's test on a per-site and per-patient basis.

**Results:** For assessment of head and neck metastases and bone metastases, accuracies of whole-body MR imaging (95.0% and 94.8%, respectively) were significantly higher than those of FDG-PET (89.1% and 88.2%, respectively; $P < 0.05$). For assessment of the M-stage on a per-patient basis, accuracy of whole-body MR imaging (80.0%) was also significantly higher than that of FDG-PET (73.3%; $P < 0.05$).

**Conclusion:** Whole-body MR imaging is an accurate diagnostic technique and may be considered at least as effective as FDG-PET for assessment of the M-stage of lung cancer patients.

**Key Words:** MR; PET; lung cancer; staging; contrast media; metastases
**J. Magn. Reson. Imaging 2007;26:498–509.**


LUNG CANCER IS the most common cause of cancer-related death among both men and women worldwide (1). Non-small-cell lung cancer (NSCLC) accounts for 80% of all lung cancers and small-cell lung cancer (SCLC) for the remainder (2). The treatment regimen for NSCLC depends on preoperative TNM (Tumor, Node, Metastasis) staging, with curative surgical resection possible for the early stages, while for the late stage chemoradiotherapy, chemotherapy, or best supportive care, is considered advisable, depending on the patients' performance status (3,4). For SCLC, on the other hand, treatment and prognosis is based on the simplified Veterans Administration (VA) staging method (limited stage, in which disease is confined to one hemithorax or radiation field vs. extensive stage, in which disease has spread outside the ipsilateral hemithorax) (5,6). Accurate tumor staging is, therefore, essential for choosing the appropriate treatment strategy, as it provides prognostic information and influences treatment options for lung cancer patients.

Typically, the standard approach to staging includes chest and abdominal computed tomography (CT), cranial CT or magnetic resonance (MR) imaging, bone scan, and, optionally, bone marrow biopsy. Because of its greater sensitivity compared with standard radiological examination for overall staging, whole-body positron emission tomography (PET) with fluorine-18 deoxyglucose (FDG) (FDG-PET) has been suggested for the detection of distant metastases in 9% to 11% of patients that conventional methods failed to identify (7–12). Whole-body FDG-PET is, therefore, commonly

[1]Department of Radiology, Kobe University Graduate School of Medicine, Kobe, Japan.
[2]Division of Cardiovascular, Thoracic, and Pediatric Surgery, Kobe University Graduate School of Medicine, Kobe, Japan.
[3]Division of Cardiovascular and Respiratory Medicine, Department of Internal Medicine, Kobe University Graduate School of Medicine, Kobe, Japan.
[4]Department of Radiology, Tenri Hospital, Tenri, Japan.
Contract grant sponsor: Eizai Co., Ltd.; Contract grant sponsor: Philips Medical Systems; Contract grant sponsor: Knowledge Cluster Initiative of the Ministry of Education, Culture, Sports, Science, and Technology, Japan.
Presented at the 14th Annual Meeting of ISMRM, Seattle, WA, USA, 2006.
*Address reprint requests to: Y.O., Department of Radiology, Kobe University Graduate School of Medicine, 7-5-2 Kusunoki-cho, Chuo-ku, Kobe 650-0017, Japan. E-mail: yosirad@kobe-u.ac.jp; yosirad@med.kobe-u.ac.jp; yoshiharuohno@aol.com
Received September 4, 2006; Accepted May 3, 2007.
DOI 10.1002/jmri.21031
Published online in Wiley InterScience (www.interscience.wiley.com).

utilized in current routine clinical practice as the whole-body imaging technique for cancer staging for all patients with suspected lung cancer.

Recently, whole-body MR imaging has been proposed as another whole-body technique for assessment of distant metastases in patients with breast cancer, malignant melanoma, pediatric malignancies, and other malignancies (13–17). In addition, some investigators have suggested that MR imaging has equal or better diagnostic capability than standard radiological examinations including contrast-enhanced CT, bone scintigraphy, and/or FDG-PET for the assessment of brain, bone, bone marrow, and adrenal gland metastases in oncologic patients (10,18–22). However, no direct comparison has been made between whole-body MR imaging and whole-body FDG-PET in lung cancer patients.

In this study, we present the hypothesis that whole-body MR imaging has potential as an alternative technique for the detection of distant metastases in lung cancer patients with a capability similar to that of FDG-PET. The purpose of the study was to prospectively and directly compare the capability of whole-body MR imaging and FDG-PET to assess the M-stage in lung cancer patients.

## MATERIALS AND METHODS

### *Subjects*

The institutional review board of our hospital approved the study and all patients were enrolled after they had been properly informed and had consented to participate in this study.

Ninety consecutive patients with pathologically diagnosed lung cancer prospectively underwent whole-body MR imaging and FDG-PET, as well as other standard radiological imaging modalities before treatment. All studies were completed in random order within three weeks of diagnosis and before treatment. Follow-up examinations were conducted for more than 20 months after treatment. The study group (mean age = 68 years, age range = 35–83 years) comprised 48 males (mean age = 67 years, age range = 44–78 years) and 42 females (mean age = 69 years, age range = 35–83 years). The final diagnosis of lung cancer was based on pathological findings of specimens, which showed that 62 patients had adenocarcinoma, 12 had squamous cell carcinoma, 11 had small cell carcinomas, and five had large cell carcinoma.

### *Whole-Body MR Imaging*

MR imaging was performed with a 1.5 T superconducting magnet (Gyroscan Intera; Phillips Medical Systems, Best, The Netherlands) using a moving tabletop and tabletop extender, and generating a longitudinal field of view (FOV) of 2000 mm and a transverse FOV of 530 mm. For every examination, whole-body MR images were obtained in the coronal and sagittal planes with a body coil and a moving table. For whole-body MR imaging, three sequences were used. One was the in-phase T1-gradient echo sequence (TR = 100 msec, TE = 4.6 msec, flip angle = 75°; matrix size = 256 × 128, reconstruction matrix size = 512 × 256, and number of excitations [NEX] = 2), with and without administration of contrast media. The second was the opposed-phase T1-gradient echo sequence (TR = 100 msec, TE = 2.3 msec, flip angle = 75°; 256 &times, matrix size = 128 , and reconstruction matrix size = 512 × 256 ), without contrast media. The third was the sequentially-reordered half-Fourier multishot short-inversion time (TI) inversion-recovery (STIR) turbo spin-echo sequence (TR = 3200 msec, TE = 60 msec, TI = 150 msec, echo train length [ETL] = 165; matrix size = 256 × 128, reconstruction matrix size = 512 × 256, and NEX = 2). Coronal and sagittal whole-body MR scans were performed at seven contiguous stations with 32–56 consecutive 8-mm slices acquired at each station. The breath holding technique was used for the thorax, with eight slices acquired on the coronal and sagittal planes for each breathhold. During contrast-enhanced whole-body MR examination, a standard dose (0.1 mmol/kg of body weight [BW]) of contrast materials (gadoteridol, Gd-HP-DO3A, or PuroHance; Eizai Co., Ltd., Tokyo, Japan) was administered intravenously via an antecubital vein. All whole-body MR examinations were performed within less than 60 minutes (mean = 53.4 minutes,; examination time range = 40–60 minutes). Images acquired in matching positions were automatically aligned to generate a seamless whole-body coronal and sagittal image with the aid of a prototype software (View Forum; Philips Medical Systems) and subjected to an interactive workstation review.

### *FDG-PET Examination*

All FDG-PET examinations were performed with a commercially available PET scanner (ALLEGRO; Philips). Patients fasted for at least six hours before the intravenous administration of FDG at a rate of 4.44 MBq/kg BW, and images were obtained from the skull through the mid-thigh 60 minutes after completion of the injection. Prior to FDG administration, a three-dimensional (3D) transmission scan was performed with Cesium-137 ($^{137}$Cs) point sources at a rate of 23 seconds/bed position. Total duration of the $^{137}$Cs transmission scan was about four minutes (scan length = 100 cm). The PET emission scan started automatically at the end point of the transmission. The 3D emission scan consisted of eight to 11 bed positions of three minutes each (150 seconds/bed position) for a scan length of 770 mm to 1020 mm and total acquisition time per patient varying from 30 minutes to 40 minutes. The patients were given no specific breathing instructions and scans were performed during quiet tidal breathing. PET images were reconstructed with the 3D row action maximum likelihood reconstruction algorithm and displayed in a 144 × 144 matrix, which contained 4.0 × 4.0 × 4.0 mm$^3$ voxels. After correction for radioactive decay, the standard uptake value (SUV) was calculated by dividing the administered FDG dose per kg/BW for each voxel, and displayed as an SUV image.

### *Standard Radiological Examinations for Initial Staging and Follow-Up Examination*

The standard imaging for M-stage assessment, both initially and during follow-up examinations, included brain MR imaging with administration of contrast media, contrast-enhanced whole-body CT, and bone scintigraphy.

#### *Brain MR Imaging*

All patients underwent brain MR imaging, with administration of contrast media, performed on a 1.5-T superconducting magnet (Signa Excite XL Echospeed; General Electronics Healthcare, Milwaukee, WI, USA) using an eight-channel HR brain coil. Brain MR images were obtained in the axial, sagittal, and coronal planes by using three sequences. One was the noncontrast-enhanced and contrast-enhanced T1-weighted spin-echo sequence (TR = 500 msec, TE = 15–20 msec, matrix size = 512 × 512, FOV = 200 msec, slice thickness = 5 mm, gap = 1 mm, and NEX = 1). Another was the T2-weighted fast spin-echo sequence (TR = 3000 msec, TE = 102 msec, ETL = 8, matrix size = 512 × 512, FOV = 200 msec, slice thickness = 5 mm, gap = 1 mm, and NEX = 1). And the third was the fluid-attenuation inversion-recovery (FLAIR) spin-echo sequence (TR = 8000 msec, TE = 100 msec, TI = 2000 msec, matrix size = 512 × 256, FOV = 200 msec, slice thickness = 5 mm, gap = 1 mm, and NEX = 1). All contrast-enhanced T1-weighted spin-echo images were obtained after administration of a standard dose (0.1 mmol/kg BW) of contrast medium (Gd-HP-DO3A). All brain MR images were interpreted by two neuroradiologists with five and nine years of experience, after which the sites of metastatic disease were recorded. Disagreements in interpretation were resolved by consensus. FDG-PET scans and whole-body MR images were not made available to the neuroradiologists at the time of interpretation.

#### *Whole-Body Multislice CT Examination*

For the one-day, whole-body, multislice CT (MSCT) examination, each patient was subjected to the following three procedures: a chest MSCT from lung apex to diaphragm during suspended respiration at the end of inspiration, an abdominal MSCT from the diaphragm to the anus during suspended respiration at the end of inspiration, and a neck MSCT from skull base to lung apex. These procedures were performed in random order with a 16-slice CT scanner (Aquilion 16; Toshiba Medical Systems, Tokyo, Japan). The instrument parameters of the chest scan were 120 kV; 150 mAs; collimation = 16 × 0.5 mm; pitch = 0.9375; and FOV = 300–350 mm. The parameters of the abdominal scan were 120 kV; 200 mAs; collimation = 16 × 1 mm; pitch = 0.9375; FOV = 300–350 mm. The parameters of the neck scan were 120 kV; 150 mAs; collimation = 16 × 0.5 mm; pitch = 0.9375; and FOV = 300–350 mm. During scanning, 100 mL of contrast material (Iopamiron 300; Schering Japan, Osaka, Japan) was administered intravenously via an antecubital vein at 2–3 mL/second by a power injector (Auto Enhance-50; Nemoto, Tokyo, Japan). All CT images were obtained with a scan delay of 20–30 seconds, and reconstructed to 5 mm contiguous slice images. All CT images were interpreted by at least two experienced head and neck, thoracic, and abdominal radiologists (with at least 10 years of experience), followed by recording of the sites of metastatic disease. Disagreements in interpretation were resolved by consensus. FDG-PET scans and whole-body MR images were not made available to the radiologists at the time of interpretation.

#### *Bone Scintigraphy*

All patients underwent radionuclide bone scintigraphy using a SPECT scanner (e-CAM; Siemens Medical Systems; Forchheim, Germany). Whole-body planar imaging in the anterior and posterior positions was performed two hours after the injection of 555 MBq (15 mCi) of technetium-99m ($^{99m}$Tc) hydroxymethylene diphosphate. Scintigraphy was performed with dual-head detectors equipped with a low-energy, general-purpose, parallel-hole collimator. All patients also underwent single photon emission computed tomography (SPECT) imaging 30 minutes after planar imaging. SPECT images were obtained at a magnification factor of 1.25 in a 64 × 64 matrix, and 64 projections were acquired at 6° intervals. The time required for acquisition of one projection was approximately 30 seconds and the full study lasted 20 minutes. All bone scintigrams were interpreted by at least two general radiologists, with at least 10 years of experience in nuclear medicine, and the sites of metastatic disease were recorded. Disagreements in interpretation were resolved by consensus. FDG-PET scans and whole-body MR images were not made available to the radiologists at the time of interpretation.

### *Final Diagnosis of M-Stage*

The final M-stage and metastasis of a given site were determined based on the results of standard imaging, pathological examinations from endoscopic, CT-guided or surgical biopsies, and follow-up examinations for more than 20 months for every patient. The lesions, which were suspected as metastases on initial radiological examinations, were diagnosed as metastases when metastatic tissues were pathologically proved or the lesions were enlarged during follow-up periods or decreased in size after treatment. The lesions, which were suspected metastases on initial radiological examinations and could not be diagnosed as metastatic sites by pathological examinations, were observed for more than 20 months, and diagnosed as nonmetastatic sites when no size changes were observed during follow-up examinations for more than 24 months or during treatment periods. The final M-stage and metastasis of a given site in each patient were made by consensus at a conference consisting of radiologists, radiation oncologists, pathologists, oncologists, and surgeons, all having more than 10 years of experience (ranging between 10 and 27 years of experience).

### Image Analysis

All images were interpreted by means of a PACS system (ShadeQuest; Yokogawa Electric Co., Ltd., Tokyo, Japan).

To determine the diagnostic capability of whole-body MR imaging for assessment of M-stage in lung cancer patients, all whole-body MR studies were prospectively interpreted by two chest radiologists, one with four years of experience and the other with 12 years of experience (H.K and Y.O). The presence or absence of metastases in the head and neck, thorax, abdomen and pelvis, and bone was assessed independently by the two radiologists. The probability of the presence of metastases on a per-patient basis was then evaluated by using a five-point visual scoring system: 1, definitely absent; 2, probably absent; 3, equivocal; 4, probably present; and 5, definitely present. The final diagnosis of M-stage on a per-patient basis was made by consensus of the two readers and the sites of metastases were recorded.

To compare the diagnostic capability of whole-body MR imaging with FDG-PET, all FDG-PET studies were prospectively interpreted by two chest radiologists with six and 15 years of experience (M.N. and D.T, respectively). Both readers also have more than two years of experience with PET. The presence or absence of metastases in the head and neck, thorax, abdomen and pelvis, and bone was assessed independently by the two readers. The probability of the presence of metastases on a per-patient basis was then evaluated the same five-point visual scoring system as for whole-body MR imaging. The final diagnosis of M-stage on a per-patient basis was also made by consensus of the two readers, and the sites of metastases were recorded.

### Statistical Analysis

A kappa statistic was used to determine the interobserver agreement for whole-body MR imaging and FDG-PET on a per-site basis in each anatomical area (i.e., head and neck, thorax, abdomen and pelvis, and bone) based on lesion-by-lesion analysis and on a per-patient basis. Because the $P$ values were exploratory in nature, no Bonferroni correction was made. Interobserver agreement was considered as slight for $\kappa < 0.21$, fair for $\kappa = 0.21$–$0.40$, moderate for $\kappa = 0.41$–$0.60$, substantial for $\kappa = 0.61$–$0.80$, and almost perfect for $\kappa = 0.81$–$1.00$ (23).

Receiver operating characteristic (ROC) curve analysis was used to evaluate the diagnostic capabilities of whole-body MR imaging and FDG-PET on a per-site basis. The sensitivity, specificity, and accuracy of the two methods were statistically compared by means of McNemar's test.

To evaluate the diagnostic capability of whole-body MR imaging and FDG-PET, ROC curve analysis was performed on a per-patient basis. The sensitivity, specificity, and accuracy of the two methods were then statistically compared by using McNemar's test on a per-patient basis.

A $P < 0.05$ was considered statistically significant for all statistical analyses.

## RESULTS

All whole-body MR and FDG-PET examinations were completed successfully, without any adverse effects being observed for any radiological examination. Details of patient characteristics are shown in Table 1. Of the 90 patients, 31 were stage I, 22 were stage II, 17 were stage II, and 20 were stage IV. Moreover, 62 sites with metastases were detected in these 90 lung cancer patients, including bone metastases ($N = 25$), lung metastases ($N = 13$), lymph node metastases ($N = 11$), brain metastases ($N = 7$), adrenal gland metastases ($N = 3$), liver metastases ($N = 2$), and intrapelvic metastasis ($N = 1$). In addition, 199 sites with other findings were identified, including osteophytes ($N = 60$), benign pulmonary nodules (except primary lesions and lung metastases) ($N = 45$), compression fractures of vertebrae ($N = 31$), renal cysts ($N = 30$), liver cysts ($N = 12$), colon polyps ($N = 8$), hemangiomas in the liver ($N = 4$), adrenal gland adenomas ($N = 4$), pancreas cysts ($N = 3$), colon cancer ($N = 1$), and rectal cancer ($N = 1$). Representative cases are shown in Figs. 1–3.

Table 1
Patient Characteristics

| | Numbers |
|---|---|
| Age (years) | |
| Mean | 68 |
| Range | 35–83 |
| Sex (cases) | |
| Male | 48 |
| Female | 42 |
| Histology (cases) | |
| Adenocarcinoma | 62 |
| Squamous cell carcinoma | 12 |
| Small cell carcinoma | 11 |
| Large cell carcinoma | 5 |
| Stage (cases) | |
| I | 31 |
| II | 22 |
| III | 17 |
| IV | 20 |
| Site-specific metastases (sites) | |
| Total | 62 |
| Brain | 7 |
| Lung | 13 |
| Liver | 2 |
| Adrenal gland | 3 |
| Lymph node | 11 |
| Bone | 25 |
| Intrapelvic | 1 |
| Other findings (sites) | |
| Total | 199 |
| Benign pulmonary nodule except primary lesion | 45 |
| Liver cyst | 12 |
| Hemangioma in the liver | 4 |
| Pancreas cyst | 3 |
| Adrenal gland adenoma | 4 |
| Renal cyst | 30 |
| Compression fracture of vertebra | 31 |
| Spondylosis | 60 |
| Colon polyp | 8 |
| Colon cancer | 1 |
| Rectal cancer | 1 |

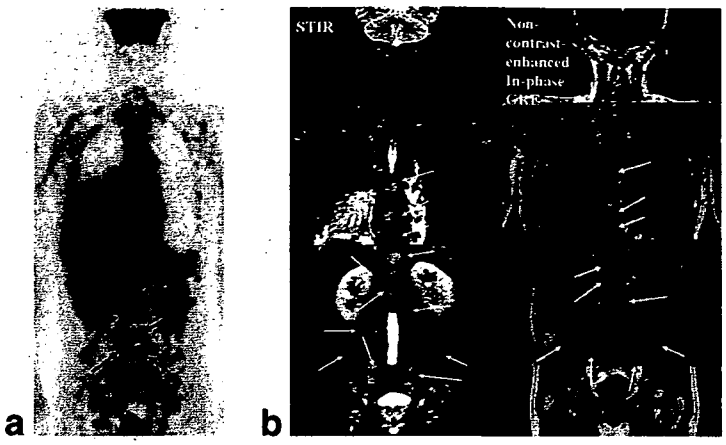


**Figure 1.** A 70-year-old man with adenocarcinoma and multiple bone metastases. **a:** FDG-PET shows multiple bone metastases (arrows). **b:** Whole-body MR also demonstrates the presence of multiple bone metastases as high signal intensities on STIR images (arrows) and low signal intensities on in-phase gradient-echo images (arrows).

The results of the scores for metastatic lesions recorded by the two readers and based on whole-body MR imaging and FDG-PET on a per-site basis are shown in Table 2. The assessments demonstrated that interobserver agreements were substantial. For whole-body MR imaging, the $\kappa$ values were 0.72 for head and neck metastases, 0.61 for thoracic metastases, 0.62 for abdominal and intrapelvic metastases, and 0.70 for bone metastases. For FDG-PET, the corresponding values were 0.63, 0.63, 0.62, and 0.72, respectively.

The actual scores are shown in Table 3. For assessment of the M-stage for lung cancer patients, interobserver agreement for whole-body MR imaging was also substantial ($\kappa$ = 0.68), as was that for FDG-PET ($\kappa$ = 0.68).

The results of ROC curve analyses of whole-body MR imaging and FDG-PET on a per-site basis are shown in Fig. 4. For assessment of head and neck metastases on per-site basis, the area under the ROC curve (Az) of whole-body MR imaging (Az = 0.97) was significantly larger than that of FDG-PET (Az = 0.68; $P < 0.05$). On the other hand, when brain metastases were excluded from head and neck metastases on a per-site basis, the area under the curve of whole-body MR imaging (Az = 0.95) had no significant difference from that of FDG-PET (Az = 0.90; $P > 0.05$). In addition, when other metastases were assessed on a per-site basis, the Azs of whole-body MR imaging (thorax: Az = 0.65, abdomen and pelvis: Az = 0.90, and bone: Az = 0.93) showed no significant differences from those of FDG-PET (thorax: Az = 0.65, abdomen and pelvis: Az = 0.93, and bone: Az = 0.90) ($P > 0.05$).

The results of a comparative analysis of the diagnostic capability of whole-body MR imaging and FDG-PET for metastatic lesions on a per-site basis and the false-positive and false-negative lesions at the sites are shown in Tables 4 and 5. For assessment of head and neck metastases, sensitivity (84.6%), and accuracy (95.0%) of whole-body MR imaging were significantly higher than those of FDG-PET (15.4% and 89.1%, respectively) on a per-site basis ($P < 0.05$). In addition, when bone metastases were assessed, specificity (96.1%) and accuracy (94.8%) of whole-body MR imaging were significantly higher than those of FDG-PET (88.3% and 88.2%, respectively) on a per-site basis ($P < 0.05$). However, when brain metastases were excluded from head and neck metastases, sensitivity, specificity, and accuracy of whole-body MR imaging had no significant difference from those of FDG-PET ($P > 0.05$). Moreover, for diagnosis of thoracic, abdominal, and pelvic metastases, the sensitivity, specificity, and accuracy of whole-body MR imaging and FDG-PET showed no

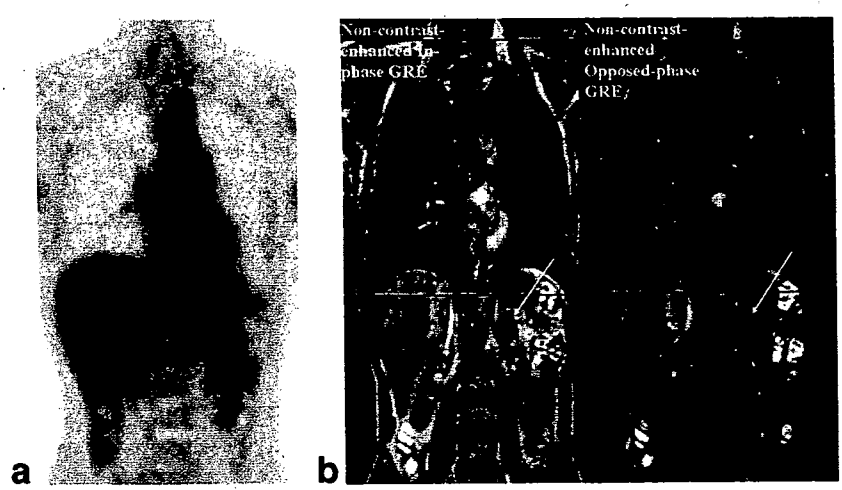


**Figure 2.** A 73-year old man with a squamous cell carcinoma and left adrenal gland metastasis. **a:** High FDG uptake on FDG-PET demonstrates a left adrenal gland metastasis (arrow). **b:** Whole-body MR imaging also demonstrates a left adrenal gland metastasis, which shows no signal reduction on dual-phase T1-weighted images (arrow).

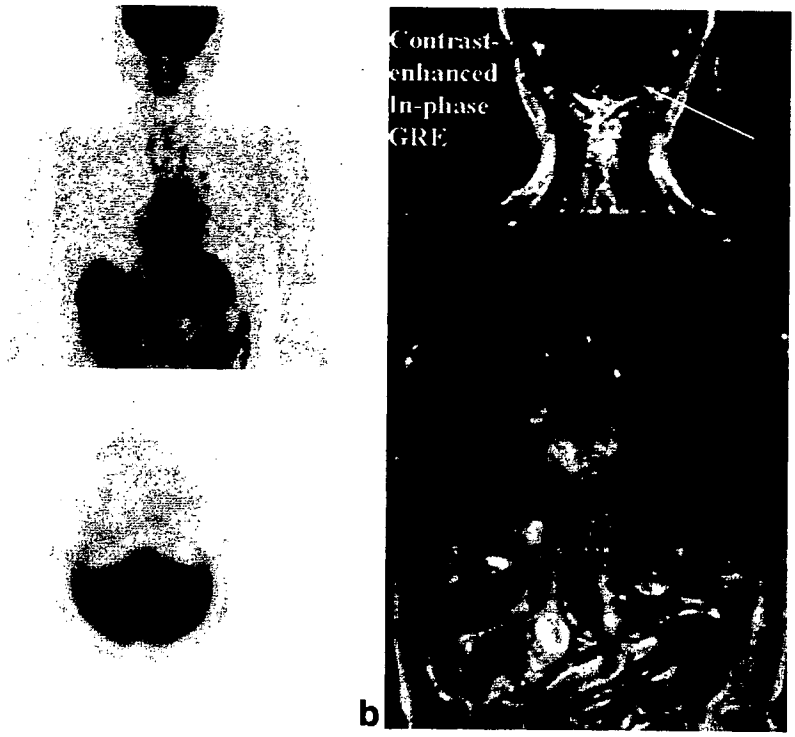


**Figure 3.** A 73-year old patient with adenocarcinoma and brain metastasis. **a:** Coronal and axial images of FDG-PET do not indicate a cerebellar metastasis. **b:** Whole-body MR imaging clearly demonstrates the presence of a cerebellar metastasis on a contrast-enhanced in-phase T1-weighted image (arrow).

significant differences ($P > 0.05$). False-positive and false-negative lesions differed from lesion to lesion and site to site.

The results of ROC curve analyses of whole-body MR imaging and FDG-PET on a per-patient basis are shown in Fig. 5. The Az of whole-body MR imaging (Az = 0.84) was not significantly different from that of FDG-PET (Az = 0.84, $P > 0.05$). Moreover, the Az of whole-body MR imaging (Az = 0.84) was also not significantly different from that of FDG-PET (Az = 0.83, $P > 0.05$), when brain metastases were excluded from head and neck metastases.

The results of a comparative analysis of the diagnostic capability of whole-body MR imaging and FDG-PET on a per-patient basis, and lists of false-positive and false-negative cases for the M-stage of lung cancer patients identified by means of the two methods, are shown in Tables 6 and 7. When brain metastases were included as head and neck metastases, accuracy (80.0%) of whole-body MR imaging was significantly better than that of FDG-PET (73.3%, $P < 0.05$). False-positive and false-negative lesions and cases differed from lesion to lesion and from patient to patient. On the other hand, when brain metastases were excluded from

Table 2
Interobserver Agreement Based on Metastatic Probability Scores for Whole-body MR Imaging (MRI) and FDG-PET (PET) on a Per-site Basis*

| | Observer | Probability score | | | | | κ |
|---|---|---|---|---|---|---|---|
| | | 1 | 2 | 3 | 4 | 5 | |
| Head and neck | | | | | | | |
| MRI | 1 | 53 | 28 | 6 | 6 | 8 | 0.72 |
| | 2 | 53 | 14 | 7 | 5 | 9 | |
| PET | 1 | 55 | 29 | 15 | 1 | 1 | 0.63 |
| | 2 | 54 | 32 | 12 | 1 | 2 | |
| Thorax | | | | | | | |
| MRI | 1 | 60 | 29 | 22 | 4 | 6 | 0.61 |
| | 2 | 59 | 30 | 21 | 6 | 5 | |
| PET | 1 | 60 | 31 | 24 | 2 | 4 | 0.63 |
| | 2 | 59 | 32 | 24 | 3 | 3 | |
| Abdomen and pelvis | | | | | | | |
| MRI | 1 | 63 | 30 | 25 | 5 | 6 | 0.62 |
| | 2 | 64 | 31 | 22 | 6 | 6 | |
| PET | 1 | 56 | 31 | 26 | 6 | 10 | 0.62 |
| | 2 | 55 | 32 | 24 | 7 | 11 | |
| Bone | | | | | | | |
| MRI | 1 | 54 | 39 | 33 | 12 | 15 | 0.7 |
| | 2 | 55 | 38 | 34 | 12 | 14 | |
| PET | 1 | 51 | 35 | 30 | 18 | 19 | 0.7 |
| | 2 | 51 | 33 | 30 | 21 | 18 | |

*For details of the probability scores, see Image Analysis under Materials and Methods. The figures below the scores refer to the number of lesions.

Table 3
Interobserver Agreement Based On Metastatic Probability Scores for Whole-Body MR Imaging (MRI) and FDG-PET (PET) on a Per-Patient Basis*

| | Observer | Probability score | | | | | κ |
|---|---|---|---|---|---|---|---|
| | | 1 | 2 | 3 | 4 | 5 | |
| MRI | 1 | 24 | 23 | 13 | 13 | 17 | 0.68 |
| | 2 | 23 | 23 | 14 | 13 | 17 | |
| PET | 1 | 23 | 23 | 13 | 16 | 16 | 0.68 |
| | 2 | 25 | 21 | 12 | 17 | 15 | |

*For details of the probability scores, see Image Analysis under Materials and Methods. The figures below the scores refer to the number of lesions.

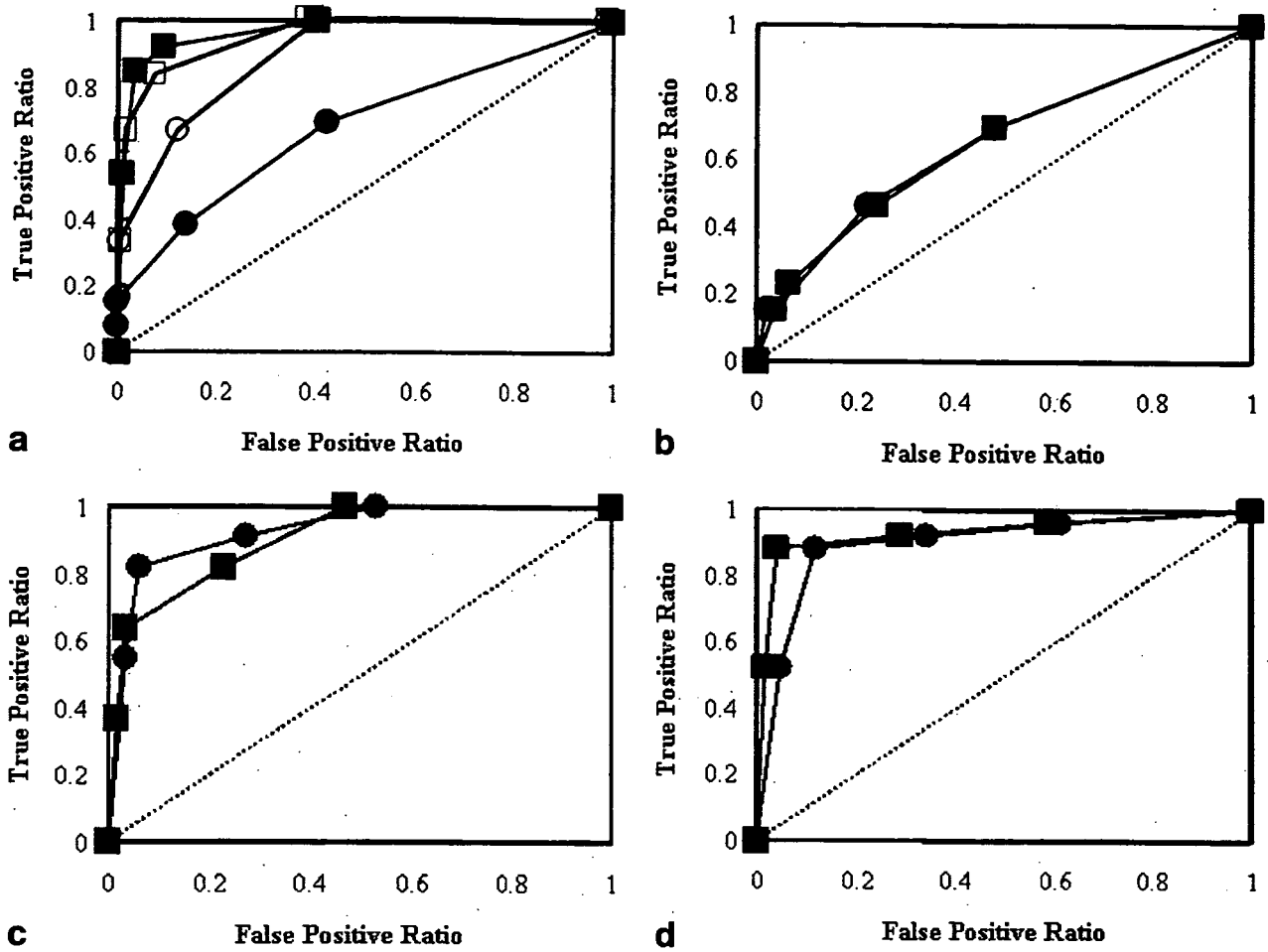


**Figure 4.** ROC curve analysis of whole-body MR imaging and FDG-PET on a per-site basis. **a:** Results of ROC curve analysis of assessment of head and neck metastasis (■: whole-body MR imaging, ●: FDG-PET) show that area under the ROC curve (Az) of whole-body MR imaging (Az = 0.97) is significantly larger than that of FDG-PET (Az = 0.68) ($P < 0.05$). On the other hand, results of ROC curve analysis of assessment of head and neck metastases except brain metastases (□: whole-body MR imaging, ○: FDG-PET) demonstrated that the area under the ROC curve of whole-body MR imaging (Az = 0.95) had no significant difference with that of FDG-PET (Az = 0.90) ($P > 0.05$). **b:** Results of ROC curve analysis of assessment of thoracic metastasis (■: whole-body MR imaging, ●: FDG-PET) indicate no significant differences between whole-body MR imaging (Az = 0.65) and FDG-PET (Az = 0.65) ($P > 0.05$). **c:** Results of ROC curve analysis of assessment of abdominal and pelvic metastasis (■: whole-body MR imaging, ●: FDG-PET) show no significant differences between whole-body MR imaging (Az = 0.90) and FDG-PET (Az = 0.93) ($P > 0.05$). **d:** Results of ROC curve analysis of assessment of bone metastasis (■: whole-body MR imaging, ●: FDG-PET) also show no significant differences between whole-body MR imaging (Az = 0.93) and FDG-PET (Az = 0.90) ($P > 0.05$).

head and neck metastases, sensitivity, specificity, and accuracy of whole-body MR imaging had no significant difference with those of FDG-PET ($P > 0.05$).

## DISCUSSION

After a tissue diagnosis of lung cancer has been established, consideration must turn to the determination of the extent of disease, or stage, because this will have a direct impact on the management of the disease and the patient's prognosis. The most significant dividing line is between those patients who are candidates for surgical resection and those who are inoperable but will benefit from chemotherapy, radiation therapy, or both in the case of non-small-cell lung cancer patients, and between those patients who are assessed as limited disease for treatment with combined chemoradiotherapy and those who are assessed as extensive disease for treatment with chemotherapy. Therefore, assessment of the M-stage in lung cancer patients is very important for determining the appropriate management of this disease. Currently, FDG-PET is in wide use as a whole-body screening tool in routine clinical practice because of its high diagnostic accuracy for the N- and M-stages in oncologic patients. Recently, whole-body MR imaging has been proposed as an alternative technique for this purpose (13–17). However, no direct comparison has been made between whole-body MR imaging and FDG-PET for lung cancer patients.

Our results demonstrated that interobserver agreements for whole-body MR imaging and FDG-PET were almost the same and substantial on a per-site and on a

Table 4
Comparison of Capability of Whole-Body MR Imaging and FDG-PET for Diagnosis on a Per-Site Basis

| | SE (%) | SP (%) | PPV (%) | NPV (%) | AC (%) |
|---|---|---|---|---|---|
| Head and neck (included brain metastases) | | | | | |
| MRI | 84.6 (11/13) | 96.6 (85/88) | 78.6 (11/14) | 97.7 (85/87) | 95 (96/101) |
| PET | 15.4 (2/13)* | 100 (88/88) | 100 (2/2) | 88.9 (88/99) | 89.1 (90/101)* |
| Head and neck (excluded brain metastases) | | | | | |
| MRI | 66.7 (4/6) | 98.8 (85/86) | 80 (4/5) | 96.6 (85/88) | 96.7 (89/92) |
| PET | 33.3 (2/6) | 100 (86/86) | 100 (2/2) | 95.6 (86/90) | 95.7 (88/92) |
| Thorax | | | | | |
| MRI | 23.1 (3/13) | 93.5 (101/108) | 30 (3/10) | 91.8 (101/110) | 86 (104/121) |
| PET | 15.4 (2/13) | 98.1 (106/108) | 50 (2/4) | 98.1 (106/108) | 89.3 (108/121) |
| Abdomen and pelvis | | | | | |
| MRI | 63.6 (7/11) | 96.6 (114/118) | 63.6 (7/11) | 96.6 (114/118) | 93.8 (121/129) |
| PET | 81.8 (9/11) | 94.1 (111/118) | 56.3 (9/16) | 98.2 (111/113) | 93 (120/129) |
| Bone | | | | | |
| MRI | 88 (22/25) | 96.1 (123/128) | 81.5 (22/27) | 97.6 (123/126) | 94.8 (145/153) |
| PET | 88 (22/25) | 88.3 (113/128)* | 59.5 (22/37) | 92.6 (113/122) | 88.2 (135/153)* |

*Significant difference with whole-body MR imaging ($P < 0.05$).
SE = sensitivity, SP = specificity, PPV = positive predictive value, NPV = negative predictive value, AC = accuracy.

per-patient basis, respectively. These findings suggest that whole-body MR imaging is as easy as FDG-PET for assessment of the presence or absence of metastatic sites in lung cancer patients on a per-site and on a per-patient basis. However, the diagnostic capabilities of the two modalities to reveal the M-stage and false-positive and false-negative lesions may differ, depending on time, from lesion to lesion and patient to patient on both a per-site and a per-patient basis.

For assessment of head and neck metastases, including brain metastases, our results showed that the Az of whole-body MR imaging was significantly larger than that of FDG-PET. In addition, sensitivity and accuracy of whole-body MR imaging (84.6% and 95.0%, respectively) were significantly higher than those of FDG-PET (15.4% and 89.1%, respectively), although three flow-related enhancements within vessels were identified as false-positive lesions on whole-body MR imaging. Some investigators have suggested that FDG-PET is not suited for the detection of brain metastasis (22,24,25) because the sensitivity of FDG-PET for detection of brain lesions is low when compared to that of standard imaging techniques. This is the result of the extremely high level of physiologic tissue accumulation of FDG in the cerebral cortex, which makes it difficult to visualize metastatic disease in brain. For routine clinical practice, therefore, CT and/or MR imaging have remained the standard imaging tests for this purpose (22,24,25).

Table 5
False-Positive and False-Negative Lesions Determined by Whole-Body MR Imaging and FDG-PET on a Per-Site Basis

| Sites | False-positive lesions | False-negative lesions | Other findings |
|---|---|---|---|
| Head and neck | | | |
| MRI | Flow-related enhancement ($N = 3$) | Brain metastases less than 5 mm in diameter ($N = 2$) | |
| PET | N/A | Brain metastases less than 10 mm in diameter ($N = 7$) | |
| Thorax | | | |
| MRI | Benign pulmonary nodules 10 mm or more in diameter ($N = 7$) | Lung metastases 10 mm or less in diameter ($N = 10$) | |
| PET | Benign pulmonary nodules 20 mm or more in diameter ($N = 4$) | Lung metastases 15 mm or less in diameter ($N = 11$) | |
| Abdomen and pelvis | | | |
| MRI | Hemangiomas in the liver 15 mm or more in diameter ($N = 4$) | Lymph node metastases 20 mm or less in diameter ($N = 4$)<br>Intrapelvic metastasis 20 mm in diameter ($N = 1$) | |
| PET | Colon polyps 20 mm or less in diameter ($N = 5$)<br>Adrenal gland adenoma 20 mm or more in diameter ($N = 2$) | Adrenal gland metastases 15 mm or less in diameter ($N = 2$)<br>Liver metastasis 10 mm in diameter ($N = 1$) | Colon cancer 25 mm in diameter ($N = 1$)<br>Rectal cancer 20 mm in diameter ($N = 1$) |
| Bone | | | |
| MRI | Compression fracture ($N = 5$) | Rib metastases ($N = 3$) | |
| PET | Osteophytes ($N = 10$)<br>Compression fracture ($N = 5$) | Rib metastases ($N = 3$) | |

N/A = not applicable.

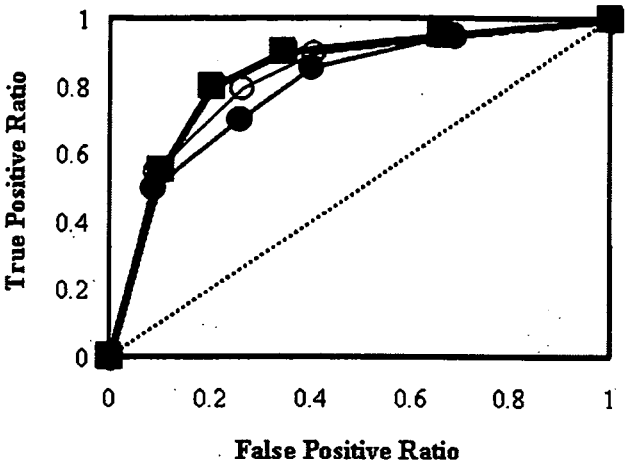


**Figure 5.** ROC curve analysis of whole-body MR imaging and FDG-PET on a per-patient basis. Results of ROC curve analysis of assessment of M-stage in lung cancer patient (■: whole-body MR imaging, ●: FDG-PET) show no significant differences in the area under the ROC curve of whole-body MR imaging (Az = 0.84) and FDG-PET (Az = 0.84) ($P > 0.05$). In addition, when brain metastases were excluded from head and neck metastases, results of ROC curve analysis of M-stage (□: whole-body MR imaging, ○: FDG-PET) also showed no significant differences in the area under the ROC curve of whole-body MR imaging (Az = 0.84) and FDG-PET (Az = 0.83) ($P > 0.05$).

Moreover, it has been suggested that contrast-enhanced MR imaging is a more sensitive screening tool for brain metastasis as compared to contrast-enhanced CT (19). Our results are, thus, compatible with those of past studies and suggest that whole-body MR imaging is the screening tool with superior diagnostic capability for assessment of brain metastases, and, therefore, cannot be replaced by FDG-PET. On the other hand, when brain metastases were excluded from head and neck metastases, the Az (Az = 0.95), sensitivity (66.7%), specificity (98.8%), and accuracy (96.7%) of whole-body MR imaging had no significant difference from those of FDG-PET (Az = 0.90, sensitivity = 33.3%, specificity = 100%, and accuracy = 95.7%). These facts suggested that whole-body MR imaging had similar capability for assessment of head and neck metastases, except brain metastases. In the present study, STIR and in-phase T1-gradient echo without contrast administration were useful for evaluation of signal intensity and short-axis diameter of cervical and supraclavicular lymph nodes and diagnosis of lymph node metastases. Therefore, the above-mentioned sequences may be useful for head and neck metastases, except brain metastases, on whole-body MR imaging. In addition, when whole-body MR imaging examines brain metastases as a part of M-stage assessment, a contrast-enhanced in-phase gradient echo sequence should be added for this purpose.

For assessment of thoracic metastasis, the Az of whole-body MR imaging was not significantly different from that of FDG-PET, based on a lesion-by-lesion analysis. In addition, a per-site–based analysis showed that sensitivities of whole-body MR imaging (23.1%) and FDG-PET (15.4%) were very low, although specificity and accuracy of FDG-PET (98.1% and 89.3%, respectively) were slightly better than those of whole-body MR imaging (93.5% and 86%, respectively). In our study, lung metastases ≤10 mm in diameter were false-negative on whole-body MR imaging ($N = 10$), due to the limited spatial resolution and those ≤15 mm in diameter were false-negative on FDG-PET ($N = 11$), due to the faint uptake of FDG. On the other hand, focal lesions ≥10 mm in diameter on whole-body MR imaging ($N = 7$) and those ≥20 mm in diameter on FDG-PET ($N = 4$) were false-positive cases. Separate metastatic nodule(s) present in the ipsilateral nonprimary tumor lobe(s) of the lung were classified as M1, according to the TNM classification. Currently, CT is the most sensitive screening tool for detection of small pulmonary nodules, so that, in routine clinical practice, assessment of metastatic nodules in terms of increase in size is usually made by means of follow-up CT examination. In view of the low sensitivity of whole-body MR imaging using STIR and non-contrast-enhanced and contrast-enhanced dual-phase T1-gradient echo sequences and FDG-PET compared to that of CT, whole-body MR imaging and/or FDG-PET may, therefore, not be suitable as the initial screening tool for identification of separate metastatic nodule(s) in the ipsilateral nonprimary tumor lobe(s) of the lung.

For assessment of abdominal and pelvic metastases, the Az of whole-body MR imaging was not significantly different from that of FDG-PET. In addition, the diagnostic capability for assessment of abdominal and pelvic metastases of whole-body MR imaging and FDG-PET showed no significant differences. In our study, false-negative lesions for whole-body MR imaging comprised four lymph node metastases and an intrapelvic

Table 6
Comparison of Diagnostic Capability of Whole-Body MR Imaging and FDG-PET on a Per-Patient Basis

| | SE (%) | SP (%) | PPV (%) | NPV (%) | AC (%) |
|---|---|---|---|---|---|
| Included brain metastases | | | | | |
| MRI | 80 (16/20) | 80 (56/70) | 53.3 (16/30) | 93.3 (56/60) | 80 (72/90) |
| PET | 70 (14/20) | 74.3 (52/70) | 43.8 (14/32) | 89.7 (52/58) | 73.3 (66/90)* |
| Excluded brain metastases | | | | | |
| MRI | 80 (16/20) | 80 (56/70) | 53.3 (16/30) | 93.3 (56/60) | 80 (72/90) |
| PET | 80 (16/20) | 74.3 (52/70) | 47.1 (16/34) | 92.9 (52/56) | 75.6 (68/90) |

*Significant difference with whole-body MR imaging ($P < 0.05$).
SE = sensitivity, SP = specificity, PPV = positive predictive value, NPV = negative predictive value, AC = accuracy.

Table 7
False-Positive and False-Negative Cases Determined by Whole-Body MR Imaging and FDG-PET on a Per-Patient Basis

| False-positive cases (cases) | False-negative cases (cases) | Other findings (cases) |
|---|---|---|
| MRI | | |
| Pulmonary nodules ($N$ = 6) | Lung metastases ($N$ = 2) | |
| Hemangiomas ($N$ = 2) | Intrapelvic metastases ($N$ = 1) | |
| Hemangiomas and renal cysts ($N$ = 2) | Bone and abdominal lymph node metastases ($N$ = 1) | |
| Pulmonary nodule and compression fractures ($N$ = 1) | | |
| Compression fractures ($N$ = 2) | | |
| PET | | |
| Pulmonary nodules ($N$ = 4) | Brain metastases ($N$ = 2) | Colon cancer ($N$ = 1) |
| Adrenal gland adenoma ($N$ = 2) | Lung metastases ($N$ = 2) | Rectal cancer ($N$ = 1) |
| Osteophytes ($N$ = 6) | Bone metastases ($N$ = 1) | |
| Compression fractures ($N$ = 3) | Adrenal gland metastases ($N$ = 1) | |
| Colon polyps ($N$ = 3) | | |

metastasis, and false-positive lesions consisted of four hemangiomas in the liver. These false-negative lesions were missed due to the difficulty of detection on the coronal or sagittal planes and, also, axial contrast-enhanced CT and FDG-PET. Moreover, four false-positive lesions proved to be heterogeneously enhanced tumors within the liver and could not be differentiated from liver metastases when whole-body MR imaging was used, although multiphase dynamic contrast-enhanced CT and FDG-PET could clearly differentiate these hemangiomas from liver metastases. These data suggest that the whole-body MR sequence used by us should be improved, to reduce the number of false-negative and false-positive lesions by adopting the multiphase dynamic T1-weighted gradient echo sequence for the axial plane, similar to the situation for multiphase dynamic axial CT. The results of our study also demonstrated that false-negative lesions of FDG-PET comprised two adrenal gland metastases and a liver metastasis, and false-positive lesions of FDG-PET comprised five colon polyps (which could not be detected by whole-body MR imaging), and two adrenal gland adenomas (which could be distinguished from adrenal gland metastases by using dual-phase T1-weighted gradient echo) as reported in the past (18, 24–26). These findings suggest that small liver and adrenal gland metastases were false-negative lesions because of the faint uptake of FDG and the difficulty of detection due to the low metabolic activity and spatial resolution of FDG-PET. In addition, a colon cancer and a rectal cancer, which were missed by whole-body MR imaging, were detected by FDG-PET only. For accurate determination of the M-stage in lung cancer patients, whole-body MR imaging is, therefore, as effective as FDG-PET for assessment of abdominal and pelvic metastases. Moreover, dual-phase T1-gradient echo sequence may be considered as useful for diagnosis of abdominal and pelvic metastases in lung cancer patients.

On assessment of bone metastases, although the Az and sensitivity of whole-body MR imaging were not significantly different from those of FDG-PET, specificity and accuracy of whole-body MR imaging (96.1% and 94.8%, respectively) were significantly better than those of FDG-PET (88.3% and 88.2%, respectively). In our study, two identical rib metastases were false-negative lesions, due to the difficulty of detection on the coronal and sagittal planes of whole-body MR imaging and faint FDG uptake resulting from low metabolic activity within the metastatic sites. In addition, five acute or subacute compression fractures due to osteoporosis were identified as false-positive lesions with both modalities, along with 10 osteophytes; whole-body MR imaging was used to differentiate these from bone metastases, which were identified as false-positive lesions on FDG-PET. In addition, we mainly reviewed STIR and non-contrast-enhanced in-phase T1-gradient echo sequences for screening, and contrast-enhanced in-phase T1-gradient echo sequence for diagnosis. Therefore, when the above-mentioned sequences were utilized, our results suggest that whole-body MR imaging constitutes a significantly specific and accurate screening tool for assessment of bone metastases and warrants being considered for adoption as the primary screening tool, and/or a complementary screening tool, for FDG-PET assessment of bone metastases in lung cancer patients.

Our comparison of the diagnostic capabilities of whole-body MR imaging and FDG-PET on a per-patient basis demonstrated that accuracy of whole-body MR imaging (80.0%) was significantly different from that of FDG-PET (73.3%), even though Az, sensitivity, and specificity of whole-body MR imaging showed no significant differences from those of FDG-PET. False-negative cases of whole-body MR imaging in our study consisted of two cases with lung metastases and one case each with intrapelvic metastasis and with bone and abdominal lymph node metastases, while the false-negative cases of FDG-PET comprised two cases each with brain metastases and with lung metastases, and one case each with bone metastases and with adrenal gland metastases. On the other hand, false-positive cases of whole-body MR imaging comprised six cases with benign pulmonary nodules, two cases each with hemangiomas, hemangiomas and renal cysts, and compression fractures, and one case with benign pulmonary nodule and compression fracture. False-positive cases of FDG-PET comprised six cases with osteophytes, four cases with pulmonary nodules, three cases each with

compression fractures and colon polyps, and two cases with adrenal gland adenomas. Only two false-negative cases with lung metastases were misdiagnosed as M0 diseases and only four cases with pulmonary nodules and three cases with compression fractures were misdiagnosed as M1 diseases by both whole-body MR imaging and FDG-PET. In addition, when brain metastases were excluded from head and neck metastases, sensitivity (80%), specificity (80%), and accuracy (80%) of whole-body MR imaging also had no significant differences with those of FDG-PET (80%, 74.3%, and 75.6%, respectively). Therefore, our results indicate that whole-body MR imaging may be at least as effective as FDG-PET as a whole-body M-stage screening tool for lung cancer, while its potential for accurate assessment of the M-stage may be even higher than that of FDG-PET.

Our study has some limitations. 1) Previous reports indicate that when a lung cancer reaches 5 mm in diameter, it has undergone approximately 20 doublings and contains about 100 million cells (27), while angiogenesis occurs in most tumors with a diameter of 1–2 mm (28,29). These findings suggest that we may have missed some doubtful metastatic sites that could not be detected by standard imaging, whole-body MR imaging, or FDG-PET. The diagnostic capability of our study is, therefore, suspected of being affected by this limitation. 2) Although we determined final M-stage and metastasis of a given site (by consensus, at a conference consisting of radiologists, radiation oncologists, pathologists, oncologists, and surgeons having more than 10 years of experience) according to the results of standard imaging, pathological examinations from endoscopic, CT-guided, or surgical biopsies, and follow-up examinations for more than 20 months, we could not pathologically diagnose the final M-stage and metastasis of a given site in every patient. This fact suggested that any sensitivity and specificity results in the present study were biased due to incomplete pathological sampling. 3) In the present study, we demonstrated that the capability for assessment of M-stage on whole-body MR imaging was similar to that on FDG-PET in lung cancer patients. However, we could not directly compare the convenience of them as a screening tool. As whole-body MR imaging, STIR sequence and dual-phase T1-gradient echo sequence with and without administration of contrast media at seven contiguous stations were obtained and reviewed for assessment of M-stage in each lung cancer patient. When considering the difference in image interpretation for M-stage assessment between whole-body MR imaging and FDG-PET, one of the major drawbacks of whole-body MR imaging is considered to be the time consumed with a higher number of images per patient than FDG-PET. Therefore, to install whole-body MR imaging in routine clinical practice, development of workstation and further investigations for determination of feasible sequences of whole-body MR imaging on a per-site basis may be warranted. 4) Although the utility of FDG-PET has been stated in many past reports, integrated FDG-PET/CT or FDG-PET with CT fusion have been suggested as having much more potential for assessment of lung cancer staging and utilization in routine clinical practice in this setting (30–34). In the present study, whole-body MR imaging was directly compared with FDG-PET, and not with FDG-PET/CT, for assessment of M-stage in lung cancer. In addition, PET examinations in the present study were interpreted without any information of CT. This fact may have influenced our results in a number of areas. Moreover, the number of patients enrolled in our study was limited for a direct and prospective comparison of the diagnostic capabilities of whole-body MR imaging and FDG-PET on a per-site and a per-patient basis; so that a large-scale prospective trial to determine the real significance of whole-body MR imaging as compared to PET/CT or PET with CT fusion for assessment of the M-stage in lung cancer patients appears to be warranted. We are now planning such a study.

In conclusion, our study showed that whole-body MR imaging is an accurate diagnostic technique and may be considered at least as effective as FDG-PET for assessment of the M-stage of lung cancer patients.

## ACKNOWLEDGMENTS

We thank Yoshiyuki Ohno, MD, PhD, MPH, Professor Emeritus, Nagoya University (Department of Preventive Medicine, Graduate School of Medicine) for his statistical advice on this manuscript.

## REFERENCES

1. Parkin DM, Bray F, Ferlay J, Pisani P. Global cancer statistics, 2002. CA Cancer J Clin 2005;55:74–108.
2. Melamed MR, Flehinger BJ, Zaman MB. Impact of early detection on the clinical course of lung cancer. Surg Clin North Am 1987;67: 909–924.
3. Deslauriers J. Current surgical treatment of nonsmall cell lung cancer 2001.Eur Respir J Suppl 2002;35:S61–S70.
4. Krupnick AS, Kreisel D, Hope A, Bradley J, Govindan R, Meyers B. Recent advances and future perspectives in the management of lung cancer. Curr Probl Surg 2005;42:540–610.
5. Zelen M. Keynote address on biostatistics and data retrieval. Cancer Chemother Rep 1973;4:31–42.
6. Clark R, Ihde DC. Small-cell lung cancer: treatment progress and prospects. Oncology 1998;12:647–658.
7. Marom EM, McAdams HP, Erasmus JJ, et al. Staging non-small cell lung cancer with whole-body PET. Radiology 1999;212:803–809.
8. Pieterman RM, van Putten JW, Meuzelaar JJ, et al. Preoperative staging of non-small-cell lung cancer with positron-emission tomography. N Engl J Med 2000;343:254–261.
9. Chin R Jr, McCain TW, Miller AA, et al. Whole body FDG-PET for the evaluation and staging of small cell lung cancer: a preliminary study. Lung Cancer 2002;37:1–6.
10. Silvestri GA, Tanoue LT, Margolis ML, Barker J, Detterbeck F; American College of Chest Physicians. The noninvasive staging of non-small cell lung cancer: the guidelines. Chest 2003;123:147S–156S.
11. Kamel EM, Zwahlen D, Wyss MT, Stumpe KD, von Schulthess GK, Steinert HC. Whole-body (18)F-FDG PET improves the management of patients with small cell lung cancer. J Nucl Med 2003;44: 1911–1917.
12. Aquino SL, Fischman AJ. Does whole-body 2-[18F]-fluoro-2-deoxy-D-glucose positron emission tomography have an advantage over thoracic positron emission tomography for staging patients with lung cancer? Chest 2004;126:755–760.
13. Walker R, Kessar P, Blanchard R, et al. Turbo STIR magnetic resonance imaging as a whole-body screening tool for metastases in patients with breast carcinoma: preliminary clinical experience. J Magn Reson Imaging 2000;11:343–350.

14. Daldrup-Link HE, Franzius C, Link TM, et al. Whole-body MR imaging for detection of bone metastases in children and young adults: comparison with skeletal scintigraphy and FDG PET. AJR Am J Roentgenol 2001;177:229–236.
15. Barkhausen J, Quick HH, Lauenstein T, et al. Whole-body MR imaging in 30 seconds with real-time true FISP and a continuously rolling table platform: feasibility study. Radiology 2001;220:252–256.
16. Mazumdar A, Siegel MJ, Narra V, Luchtman-Jones L. Whole-body fast inversion recovery MR imaging of small cell neoplasms in pediatric patients: a pilot study. AJR Am J Roentgenol 2002;179: 1261–1266.
17. Lauenstein TC, Goehde SC, Herborn CU, et al. Whole-body MR imaging: evaluation of patients for metastases. Radiology 2004; 233:139–148.
18. Korobkin M, Lombardi TJ, Aisen AM, et al. Characterization of adrenal masses with chemical shift and gadolinium-enhanced MR imaging. Radiology 1995;197:411–418.
19. Yokoi K, Kamiya N, Matsuguma H, et al. Detection of brain metastasis in potentially operable non-small cell lung cancer: a comparison of CT and MRI. Chest 1999;115:714–719.
20. Earnest F, 4th, Ryu JH, Miller GM, et al. Suspected non-small cell lung cancer: incidence of occult brain and skeletal metastases and effectiveness of imaging for detection—pilot study. Radiology 1999; 211:137–145.
21. Remer EM, Obuchowski N, Ellis JD, Rice TW, Adelstein DJ, Baker ME. Adrenal mass evaluation in patients with lung carcinoma: a cost-effectiveness analysis. AJR Am J Roentgenol 2000;174:1033–1039.
22. Rohren EM, Provenzale JM, Barboriak DP, Coleman RE. Screening for cerebral metastases with FDG PET in patients undergoing whole-body staging of non-central nervous system malignancy. Radiology 2003;226:181–187.
23. Svanholm H, Starklint H, Gundersen HJ, Fabricius J, Barlebo H, Olsen S. Reproducibility of histomorphologic diagnoses with special reference to the kappa statistic. APMIS 1989;97:689–698.
24. Griffeth LK, Rich KM, Dehdashti F, et al. Brain metastases from non-central nervous system tumors: evaluation with PET. Radiology 1993;186:37–44.
25. Rohren EM, Turkington TG, Coleman RE. Clinical applications of PET in oncology. Radiology 2004;231:305–332.
26. Vansteenkiste JF. PET scan in the staging of non-small cell lung cancer. Lung Cancer 2003;42:S27–S37.
27. DeVita VT Jr, Young RC, Canellos GP. Combination versus single agent chemotherapy: a review of the basis for selection of drug treatment of cancer. Cancer 1975;35:98–110.
28. Liotta LA, Kleinerman J, Saidel GM. Quantitative relationships of intravascular tumor cells, tumor vessels, and pulmonary metastases following tumor implantation. Cancer Res 1974;34:997–1004.
29. Rak JW, St Croix BD, Kerbel RS. Consequences of angiogenesis for tumor progression, metastasis and cancer therapy. Anticancer Drugs 1995;6:3–18.
30. Antoch G, Stattaus J, Nemat AT, et al. Non-small cell lung cancer: dual-modality PET/CT in preoperative staging. Radiology 2003; 229:526–533.
31. Shim SS, Lee KS, Kim BT, et al. Non-small cell lung cancer: prospective comparison of integrated FDG PET/CT and CT alone for preoperative staging. Radiology 2005;236:1011–1019.
32. Halpern BS, Schiepers C, Weber WA, et al. Presurgical staging of non-small cell lung cancer: positron emission tomography, integrated positron emission tomography/CT, and software image fusion. Chest 2005;128:2289–2297.
33. Bruzzi JF, Munden RF. PET/CT imaging of lung cancer. J Thorac Imaging 2006;21:123–136.
34. Endo K, Oriuchi N, Higuchi T, Iida Y, et al. PET and PET/CT using (18)F-FDG in the diagnosis and management of cancer patients. Int J Clin Oncol 2006;11:286–296.

# TRON

*1ユトレヒト大学、*2フィリップスエレクトロニクスジャパン、
*3東海大学医学部付属病院診療技術部放射線技術科
高原 太郎*1、荻野 徹男*2、奥秋 知幸*2、
堀江 朋彦*3、室 伊三男*3、Marc Van Cauteren*2

## TRONの概念

TRONは、TRacking Only Navigatorの略で、呼吸同期法のひとつであるNavigator法の一種である。上腹部拡散強調画像に適応があり、撮影時間の延長がほとんど起こらずに呼吸同期効果が得られるという特長がある。

**TRON法**
TRaking Only Navigator法
上腹部拡散強調画像に用いる
撮像時間の延長がほとんどない呼吸同期法

## 拡散強調画像とMPG

拡散強調画像の骨格をなしている撮像法はT2強調画像である。通常最初のエコーをSE法で獲得し、その後のエコーをEPI法で取得するので、SE-EPI法によるT2強調画像ということになる。SE法では180度パルスを用いるが、この両側に大きな勾配磁場をかけると、拡散強調画像が得られる。静止組織は、最初の勾配磁場で位相がずれるが、次に与えられる180度パルスに続いて同じ勾配磁場をかけると、ずれたのと同じだけ位相が戻るため、位相の乱れが起こらない。この結果、T2強調画像(勾配磁場を用いないとき)と比較して、大きな信号変化は起こらない。一方、勾配磁場をかけている間に動く組織ではこれは成り立たない。

**勾配磁場**は、周りに置かれたコイルに一時的に電流を流すことにより、一瞬だけ付加される磁場である。空間的に一方の磁場強度が弱く、他方の磁場強度が強くなる状態が作られるが、この様子を、横軸を位置、縦軸を磁場強度にしたグラフで表現すると、傾斜した線で表されるので勾配磁場と呼ばれる。勾配磁場が発生している時、もし組織が動いているなら、位置の変化につれて受ける磁場の強さが変化する。磁場の強さが異なれば、スピンの歳差運動の速さも比例して変わる。

周囲の静磁場に対して生じている速さ(ラーモア周波数)に、勾配磁場により受けた磁場の強さに応じた速さの変化が一時的に加わるので、勾配磁場を受けている時間に応じただけスピンは速く回り、その結果スピンの示す**回転角(位相)**は進

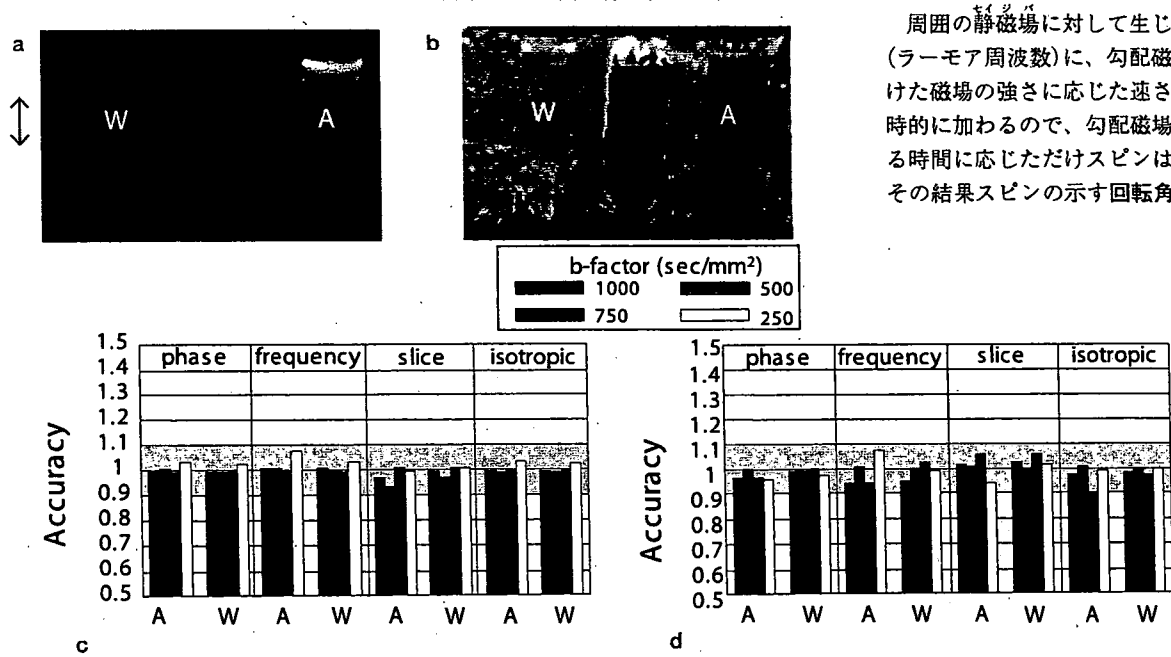


**図1 動体ファントム実験(1)**
a:DWI画像、b:ADC画像、c、d:各MPG方向及び3軸合成におけるADC値(静止ファントムにおけるADC値を1とし、動体ファントムにおけるADC値を相対値で"accuracy"として示す)。
cは10mm/sec、dは20mm/sec。いずれもストローク量20mm。ファントムの運動方向はこの紙面の天地方向。この方向ではADC測定誤差がほとんど無いことが分かる。
A:中性洗剤、W:水。
(文献2より引用)

む。対象が移動する場合、最初の勾配磁場による位相の進みと、2回目の勾配磁場による位相の戻り量は、受ける磁場強度が異なる結果不一致になり、位相は元に戻らない。ランダムに動く組織では、ひとつひとつのスピンのもつ位相がさまざまにずれる(乱れる)。この結果、総和としての位相は乱れ(dephase)、信号が低下すると考えられる。このように勾配磁場によって動きのありなしを信号低下の程度で表現できるので、この勾配磁場を、動きを検出する勾配磁場(Motion Probing Gradient：MPG)と呼んでいる。

**大きな勾配磁場をかけると、顕微鏡で倍率をあげてみるのと同じように、小さな位相ずれ(つまり小さな動き)による信号減少を記録できるようになり、水分子の拡散の程度も判断できるようになる。**つまり拡散(ランダムな水分子の運動)が小さい組織においては信号低下が起こりにくく、拡散が大きい組織においては信号低下が起こりやすい。癌や、粘稠な液体(膿瘍など)は前者に属するので、拡散強調画像において信号が残りやすい。それ以外の多くの組織は大きく信号を失う。このため、通常のT2強調画像にも増して、病変部分が特に強調された画像が得られやすい。

では、腹部における呼吸運動はこの勾配磁場(MPG)によりどのような信号低下を示すのであろうか。

## 自由呼吸と拡散強調画像の関係

自由呼吸と拡散強調画像の関係は、DWIBS(Diffusion weighted Whole body Imaging with Background body signal Suppression)で実証的に示されている。すなわち、意外なことに、「動きを検出する勾配磁場(MPG)」を用いて自由呼吸下に拡散強調画像を撮影したときに、自由呼吸による信号低下は起こらないのである。ともすると、「MPGは顕微鏡の高倍率のようなものであるから、拡散のような小さい動きでも検出(信号低下)する。だから自由呼吸が関与すれば信号は当然低下するし、そもそも正確な拡散のデータは得られない」と考えがちであったが、事実は異なっていた。筆者はこのことに気づき、従来呼吸停止か呼吸同期が必須と考えられていた腹部の拡散強調画像が、**実は自由呼吸下に撮影しても信号低下は起こらないこと、また撮影時間に制限がなくなることから、撮影時間を長くすることによりS/Nが良くなり、今までより薄いスライスでも撮影ができ、3次元的なデータセットとして拡散強調画像を扱えることを報告した[1]。**

その後、宗らにより、この臨床的観察事実は、**動体ファントム実験**で確かめられた。彼の実験結果は日本技術会雑誌に掲載されている[2]。本稿ではこの論文から2つの図を引用する(**図1、2**)。両図共に、左から各々水、脂肪、中性洗剤を入れた円筒状のファントムを撮影している。周囲はゲルで囲んである。**図1**は、この断面図に対し、ページの天地方向にファントムを動かしたときに生じるADC(拡散速度)計測結果である。ファントムが静止しているときのADCを1とし、その相対値がAccuracyとして表示されており、左下の図が10mm/sec、右下の図が20mm/secで動かしたときの結果である。いずれも1に近く、動いていてもADC測定結果が変わらないことが分かる。

このことからわかるように、**呼吸運動が動体ファントムのような等速直線運動と見なせる場合には、拡散の測定には修飾が起こらない**のである。これはどうしてかというと、運動がランダムな動きではなくて、一定方向だからである。一つの画素(ボクセル)のなかのスピンがみな一定方向の動きで修飾されるので、これ

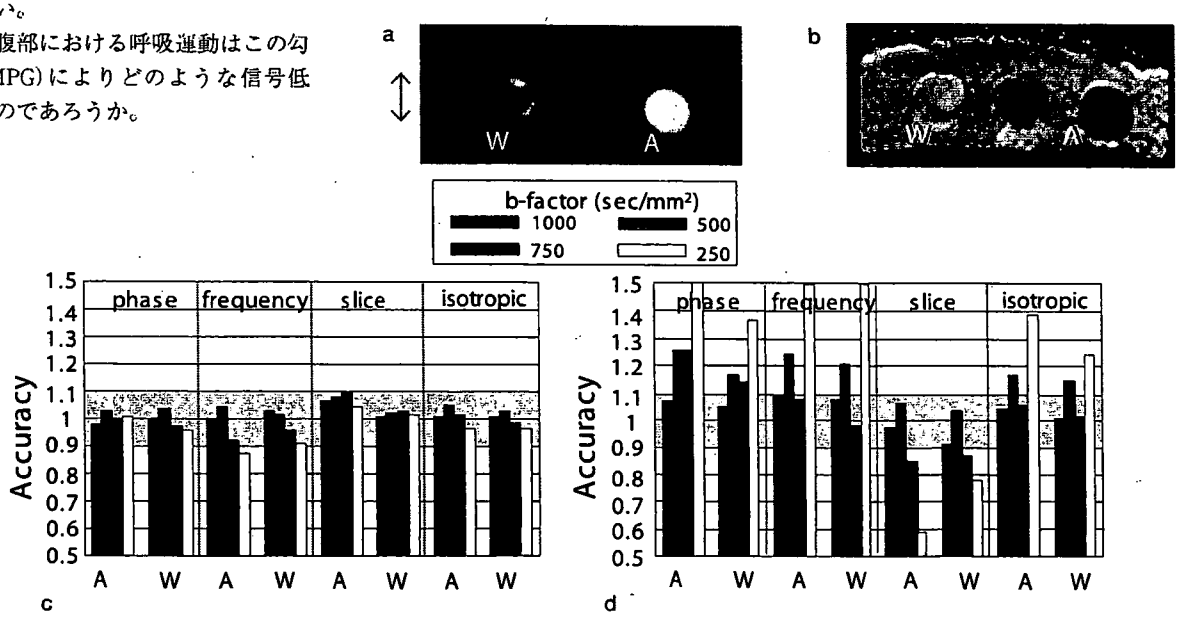


**図2　動体ファントム実験(2)**
a～dに関しては図1と同じ。
ファントムの運動方向はこの紙面の天地方向。dではADC値は過大もしくは過小を示している。理由は本文参照。　(文献2より引用)

はそれぞれのスピンに同じ量の位相変化を引き起こす。このため、お互いの**位相の乱れは起こらず、結果としてベクトル量が変わらないので信号が変化しない。**このため、ボクセル内のランダムな動き(つまり拡散)のみを検出し得るというわけである。一方、心拍動などはランダムな動き(IVIM)を生じるので修飾(信号低下)を生じる。**大切なことは運動をcoherent motionとincoherent motionに分けて考えることである**[3]。つまりMPGは、本当は"IMPG"とでも記載すべきものなのだ。

では今度は図2について解説する。図2もこの断面図に対し、ページの天地方向にファントムを動かした結果である。この場合は、速度が大きいと1から逸脱して誤差ができることがわかる。

どうして図2では誤差が出るのであろうか。それは、周囲のゲルの信号が混入したからである。つまり動き(というよりもここではMPG印加時間内に生じる**変位が大きくなること)に基づく部分容積効果**と考えることができる。実際の臨床では、動きにともなう「ぶれ」が、このようなADCの測定誤差を生み出すものと考えられる。この現象は、従来のT2WIなどでの撮像における状況と全く同じものであり、この対策として呼吸同期法が存在している訳だ。**重要なのは、図1と図2で考察できることは、異なる2つの事柄であるということである。**この2つが混同されることにより、「DWIBSでは自由呼吸OKと言っている(注：図1に相当する事実)。しかし上腹部では呼吸同期が必要だ(注：図2に相当する事実)」と言ったような、誤解を招きやすい表現方法が時に見られる。賢明な読者にはこれがナンセンスな短絡であることがもうお分かりであろう。再度まとめをコラムに示す。この2つを正確に理解し弁別することがTRONにつながるのである。


図3　拡散強調画像における呼吸同期の効果
肝転移症例。T2強調画像と同様に呼吸同期でブレを軽減することができる。

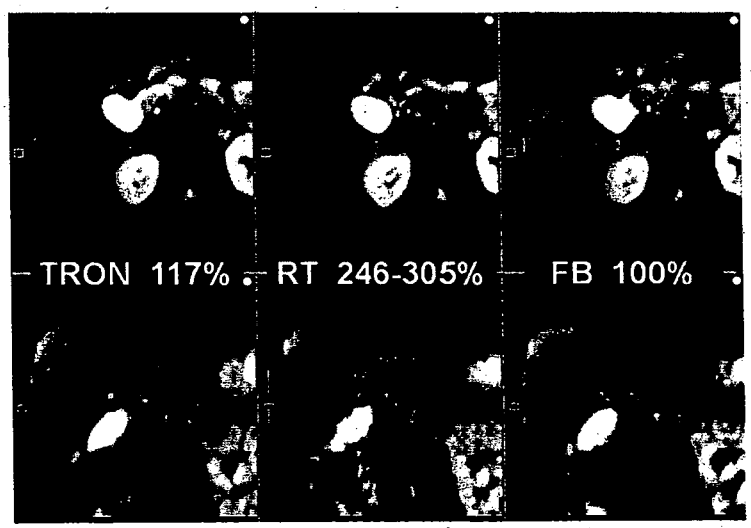


図4　TRON、RT(従来法呼吸同期)、FB(自由呼吸)の比較
%は自由呼吸を基準としたときの相対撮影時間。冠状断再構成像で、FBのぼけ、及びRTの同期不良を認め、この例ではTRONが最良の結果を示している。但しこのような明確な差があっても、ここで示すように「差の乏しいAxial像」を選びだすのは容易である。Axialで示すことが如何に危険かが分かるであろう。

**DWIBSと呼吸同期：TRONを考えるためのまとめ**

呼吸運動は、等速直線運動に近似できると仮定すると、MPGによって信号低下は生じない。だからDWIBS法のように自由呼吸下多加算撮影を行うと、それに応じただけのS/Nが得られる。→これはthin slice撮影立体表示に使うことができる。

上記の観点では、DWIもT2WIも同じ撮像法である。だから上腹部における呼吸に伴うブレは等しく発生する。従い両者共呼吸同期、理想的には呼吸停止でスキャンするのが望ましい。

## 呼吸同期の必要性とその問題

前項で述べたとおりMPGは、自由呼吸が等速直線運動に近似できると考えた場合、拡散の測定誤差は生じない。しかし臨床上、像のぼけが生じるので、結果として拡散強調画像上の病変はぼけるし、またそのADC値もかならずしも正確ではなくなる。もうすこしわかりやすく例を示すと、「T2強調画像は、静止した対象を撮影しても、呼吸運動下の対象を撮影してもT2強調画像であり、そのコントラストには変化が起こらない。しかし動きによる像のぶれは発生する」という文章と、「拡散強調画像は、静止した対象を撮影しても、呼吸運動下の対象を撮影しても拡散強調画像であり、そのコントラストには変化が起こらない。しかし動きによる像のぶれは発生する」という文章は同義である、ということである。これがDWIBSで観察した事実であり、従来、「拡散強調画像は、動いている対象を撮

影したら拡散強調画像でなくなり、信号強度が脚色されてしまう」と想像されていたことは誤りであると分かったのである。

自由呼吸下に撮影すれば、動きによる像のぶれは発生する。このため、一般に上腹部において呼吸同期で撮影することが好まれて用いられている(図3)。しかし**呼吸同期は拡散強調画像だから必要なのではなくて、T2強調画像で必要なことを同様に行って、よりシャープな画像を得ようとする努力に他ならない。**

ここまで考えを進めれば、T2強調画像において観察される呼吸同期の問題と、拡散強調画像において観察される(べき)呼吸同期の問題は同じであることが分かる。つまり、その問題は、①撮影時間が延長してしまうこと(これは多くの人の予想(=約2倍)よりも大きく、実測では3倍近い)、そしてもうひとつは、②呼吸同期が正確ではないこと、の2点である。①に関しては、皆異論のないところであろう。②に関しては、T2強調画像ではそれが生じた場合はっきりと認識できるが、拡散強調画像ではよく分からないことも多い。これは主要な背景信号が抑制されてしまっているためである。だから、**実際には不正確なのにそれを判断できないという問題がある。**内税表示の天プラを見て、税金(アーチファクト)のことに考えが及ばないようなものである。しかし**冠状断再構成画像を作成すると、これが「外税表示」のようになり、非常によく観察できるようになる(図4)。**

## TRONのコンセプト

さて話をTRONに戻そう。前項で示したごとく、「MPGは自由呼吸下で印加しても、拡散の測定に影響を生じない(DWIBSの撮像原理)」という事実と、「対象のぶれによる不正確な画像が取得される」という事実が、異なる2つの事柄であると考えると、TRONのコンセプトに近づくことができる。

呼吸同期法のひとつNavigator法は、2つの機能を有しており、それはGate & Trackである。**Gating**は、**図5**のように、Gating Windowを設定しておいて、横隔膜の位置がこの間に入った場合にデータをacceptし、他のデータをrejectする。このrejectがたくさんあるほど(Gating Windowが狭いほど)データは正確になるが、そのぶん捨てるデータが増えるので撮像時間が延長する。さらに、患者が途中で寝てしまったりすると、横隔膜のストローク範囲が完全にGating Windowから逸脱してしまい、検査中断の懸念もある。もうひとつの機能、**Tracking**は、Gating Window内のデータもwindow幅ぶんの誤差があるので、位置合わせを行って撮影する機能である。この機能により、より正確に撮影ができることになる。

前段落で述べたNavigatorの機能と、本項の初段落で述べた事柄には類似性があることに読者はお気づきであろう。つまりDWIBSの原理を用いれば、**横隔膜が動いているときにも撮影はできるのだから、位置補正にすこし誤差がでるかもしれないが、Gating Windowを撤廃しても大丈夫だろうという推論が成り立つ。**そして、Trackingの機能を用いれば、概ね正確な位置を測定できるという期待が生じるわけである。

2005年のMR学会シンポジウムなどで呼吸同期の問題がとりあげられたときに

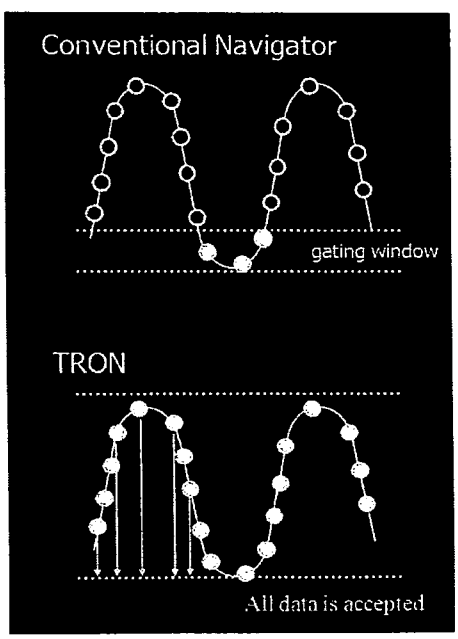


**図5　通常のNavigator法とTRONの概念**
TRONはgatingの概念を捨て全てのdataをacceptする。

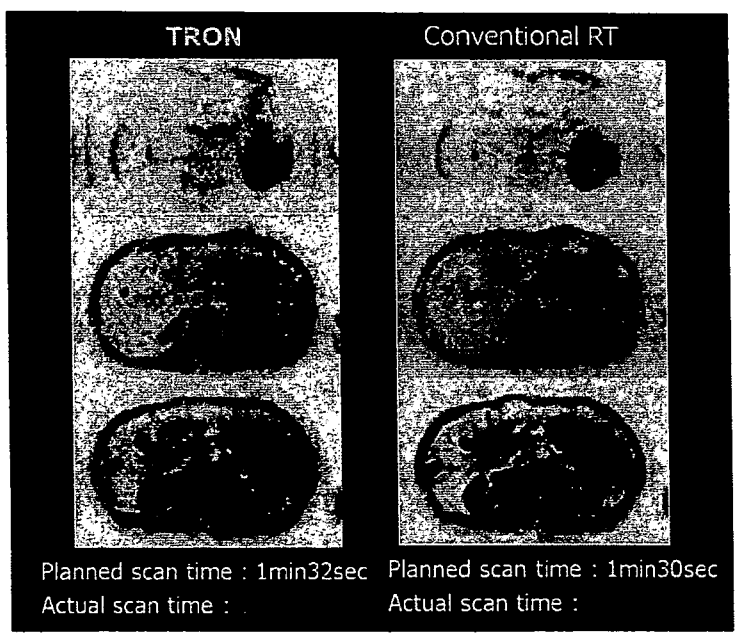


**図6　TRONと従来法呼吸同期の比較**
肝転移症例。TRONは右の従来同期と同様に3つの病変を描出している。TRONのS/Nが低いが、これはRTが非常に長いTRになってしまったことに由来する(実撮像時間)。TRONは設定撮像時間と同程度で終了している。実際の臨床ではTRONが使い易いはずである。

はすでにこのアイデアはあったが、完成前に公にするわけにもいかず歯がゆい思いをしたものである。実際のシークエンスができ、さまざまな困難を排除するのにはとても時間がかかり、ようやく2006年のMR学会で発表が可能になり、現在では時間短縮と精度の向上が図られるに至っている。これは、荻野氏、奥秋氏はじめフィリップスエレクトロニクスジャパンのMRIチーム全員の議論と努力の賜物である。筆者自身、構想を練ってからこのような長いスパンで作成していただくのははじめてのことであり、一応の完成をみてこれからβ版がいくつかの病院に配布されるようになるところまで来たのは感無量である。TRONによる臨床的なデータについてはまだ蓄積が十分ではない(一例を図6に示す)が、今後いろいろな面白い結果が得られるものと楽しみにしている。

## Pseudo-anisotropy、DWI-SBAPとTRON

本年4月の放射線学会総会で、国立がんセンター東病院(現 筑波大学)の那須克宏先生から、非常に面白い発表がなされた。それはPseudo-anisotropy(シュード・アナイソトロピー)と那須先生が呼んでいるものである。彼は、呼吸同期法で撮影された各MPG印加軸の画像を注意深く観察し、呼吸同期であっても信号低下を生じている部位があること、これは(肝臓が文字どおり硬い)肝硬変患者では頻度が少ないが、正常肝ではより高頻度に認められることを観察した。そしてCine MRIによる観察も加え、「呼吸運動により肝臓の各部位で回転運動など(coherent(コヒーレント)でない運動)が起こる」と帰結した。またこれを実証するために、DWI-SBAP(デュイ・スバップ)(本誌特集1、那須先生の記事参照)と呼ばれる撮影法(ひとことでいえば、各軸それぞれを呼吸停止で撮影し、最終的に合成する方法)により非常に精度の高いADC測定が期待できることを示した。(尚、これを理解するために論文2)の回転ファントム実験結果も是非読んで欲しい)。

これは新しい事実の観察であり、賞賛に値する。今後、このアイデアは、肝硬変の程度を観察すること(MR-Elastgraphy(エラストグラフィー)のように)や、正確な肝臓画像診断を行うにおいての記念碑となるかもしれない。今後、この領域はさらに深く研究されるものと思う。

では、**TRONは、DWI-SBAPと比較して不正確であり、役立たないのであろうか。**この結論を出すには時期尚早だが、私は決してそうではないと考えている。その理由として、那須先生が発表で述べられているように、まずtrace(トレース)画像(各軸の画像を合成した画像)ではこのアーチファクトは(視覚的には)あまり目立たないことが挙げられる。他方、図7に示すとおり、拡散強調画像は、**肝左葉外側区の描出不良という必ず発生する問題**を抱えており、これは心電図同期しない限り解決できないと信じられる。しかし心電図同期はかなり時間的に難しく、うまくできたとしても通常の3倍の時間を要する。呼吸同期で3倍、心電図同期で3倍かかるとすれば、同時の同期は9倍かかることになり、これでは全く非現実的である(表1)。DWI-SBAPにおいても、心電図同期を併用して呼吸停止で撮影するのは不可能に近い。このため、**TRONは心電図呼吸同時同期スキャンに今のところ最も近い位置にいる**と考えられるのである。またTRONは走ってしまえば基本的には追加操作や声かけを要さない手間のかからない方法なので、この点でも臨床に供しやすいというメリットがあると思われる。

TRONにはいくつかの欠点もある。それは肝臓に対するTrackingを行うが、静止部分はぼけるということである。つまり自由呼吸における肝臓のぶれと同じ事が静止組織に生じる。しかしこれは、肝臓が標的臓器となる検査においては(自由呼吸法でもあまり大きな問題がないことが多いように)、それほど重要な事実ではないと考えるし、時間とのトレードオフはどのような方法においても常に生じるからである。しかしこれは、今後の臨床応用において再検討されるべきであろう。なお、これを補正することは将来可能になると考えている。

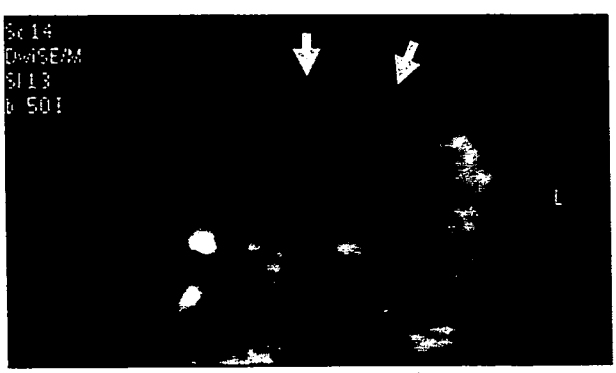

図7 肝左葉外側区の信号低下。冠状断再構成像

表1 PPU(脈波同期)とRT(呼吸同期)に必要な撮像時間
同時同期では通常の9倍もの時間を要する。

| | PPU | RT/TRON | Scan Time |
|---|---|---|---|
| PPU | 3× | — | 3× |
| Conv.RT + PPU | 3× | 3× | 9× |
| TRON + PPU | 3× | 1.1× | 3.3× |

＜文献＞
1) Takahara T, Imai Y,Yamashita T, et al: Diffusion weighted whole body imaging with background body signal suppression(DWIBS): technical improvement using free breathing, STIR and high resolution 3D display. Radiat Med 22(4): 275-282, 2004
2) 室 伊三男、高原太郎、堀江朋彦ほか:自由呼吸下一躯体部拡散強調画像における動きの影響について(動体ファントム実験). 日本放射線技術学会雑誌 61(11): 1551-1557, 2005
3) Koh DM, Takahara T, Imai Y, et al: Practical aspects of clinical diffusion-weighted imaging in the body for tumor assessment. Magn Reson Med Sci(in press)

Magn Reson Med Sci, Vol. 6, No. 4, pp. 211-224, 2007

REVIEW

# Practical Aspects of Assessing Tumors Using Clinical Diffusion-weighted Imaging in the Body

Dow-Mu KOH[1]*, Taro TAKAHARA[2,3], Yutaka IMAI[2], and David J COLLINS[1]

[1]*CR UK Clinical Magnetic Resonance Research Group, Institute of Cancer Research and Academic Department of Radiology, Royal Marsden Hospital Downs Road, Sutton SM2 5PT, UK*

[2]*Department of Radiology, Tokai University Hospital, Japan*

[3]*Division of Radiology, Radiotherapy and Nuclear Medicine, University Medical Centre, Utrecht, Netherlands*

(Received July 23, 2007; Accepted September 5, 2007)

Diffusion-weighted magnetic resonance (MR) imaging (DWI) is increasingly applied to evaluate tumors in the abdomen and pelvis. However, DWI is susceptible to a variety of artifacts that arise from motion, use of strong gradient pulses, and echo-planar imaging technique. We discuss practical issues to help radiologists optimize the use of DWI to evaluate tumors in the body, including breath-hold DWI, multiple-acquisition non-breath-hold DWI, and diffusion-weighted whole-body imaging with background body signal suppression (DWIBS). Considerations of meticulous technique, sequence optimization, and quality assurance are emphasized for consistent acquisition of high quality images. We illustrate the potential use of these techniques to detect and characterize tumors and to monitor treatment effects.

**Keywords:** ***magnetic resonance imaging, diffusion, technique***

## Introduction

Diffusion-weighted magnetic resonance imaging (DWI) probes the diffusion of water in the body. The motion of water molecules in the extra- and intracellular spaces and intravascular space contributes to the net water displacement measured by DWI. The technique yields qualitative and quantitative information that reflects tissue cellularity and cell membrane integrity and thus complements morphological information obtained by conventional MR imaging.

Performing DWI in the body is challenging because the inhomogeneity of the magnetic field over a large imaging area and motion arising from different organs conspire to degrade image quality. In the past decade, a series of technological advancements in MR imaging, including higher amplitude gradients, echo-planar imaging (EPI), parallel imaging techniques, and the use of respiratory gating and cardiac triggering for motion compensation, has helped overcome many of these issues. Of these, the development of parallel imaging has been critical because its enables use of very short echo time and reduced echo-train length for very quick acquisition of images with good signal-to-noise that are relatively undegraded by motion and local field gradients.

High quality DWI images can be routinely obtained using modern 1.5T MR imaging systems from the major manufacturers (e.g., General Electric, Milwaukee, USA; Siemens, Erlangen, Germany; Philips, Eindhoven, The Netherlands). However, implementation of DWI sequences differs among manufacturers, and the reader should be familiar with the strengths and limitations of their own imaging systems to optimize imaging performance. In this regard, the radiologist should work closely with the physicist and technologist in establishing scanning protocols to ensure acquisition of images of consistently high quality.

We discuss the advantages and disadvantages of commonly applied DWI strategies in the body and important considerations for image optimization to ensure high quality images for qualitative visual assessment or quantitative analysis, and we illustrate the potential use of these techniques to detect and

*Corresponding author, Phone: +44-208-661-3340, E-mail: dowmukoh@icr.ac.uk

characterize tumors and to demonstrate treatment response. We assume knowledge of and will not discuss the basic principles of DWI.[1]

## DWI Imaging Strategies in the Body

DWI imaging in the body is frequently performed using modified single and dual spin-echo sequences with the application of motion-probing gradients placed on either side of the 180° refocusing pulses. This is combined with echo-planar imaging (EPI) readout and parallel acquisition techniques (e.g. SENSE, GRAPPA) to minimize imaging time, thus preserving image signal-to-noise and reducing motion-related artifacts, without significantly impacting apparent diffusion coefficient (ADC) calculations.[2]

Current widely used imaging strategies for DWI in the body include: (1) breath-hold single-shot DWI, (2) non-breath-hold multiple averaging DWI, and (3) non-breath-hold multiple averaging DWI performed at multiple body stations (diffusion-weighted whole-body imaging with background body signal suppression [DWIBS]). Although each of these strategies is suitable for general imaging of the abdomen and pelvis, the selection of imaging sequence may be influenced by the anatomical region being investigated, whether the images are to be analyzed qualitatively or quantitatively, and the size and heterogeneity of lesions evaluated. Table summarizes typical examples of these imaging approaches.

*Breath-hold single-shot DWI.* The key advantage of using breath-hold single-shot DWI is the short image acquisition time. For example, the entire liver can be evaluated over 2 breath-holds, each lasting only 20 s. Combining parallel imaging and single-shot EPI measurements allows very short echo times (e.g., 45 to 75 ms), thereby preserving signal-to-noise.[3,4] Furthermore, breath-hold single-shot DWI would be theoretically more effective in characterizing lesion heterogeneity (e.g., on a pixel-by-pixel basis) and in quantifying the ADC of smaller lesions because such information is less likely to be degraded by the volume averaging that occurs with free-breathing techniques.

However, single-shot measurements are inherently noisy because of the low signal-to-noise of the source data. Although artifacts arising from breathing motion are reduced, pulsatile motion from the heart and the aorta can still induce artifacts. Therefore, some advocate combining this technique with cardiac pulse triggering to improve image quality and ADC calculation.[5] However, the use of pulse triggering increases image acquisition time and may render the images more prone to bulk motion. Cardiac pulsation artifacts have been shown to increase ADC measurement in the left lobe of the normal liver compared with the right lobe.[6] The need for good signal-to-noise also means that breath-hold imaging may require thicker slice partitions (6 to 8 mm). Another potential disadvan-

**Table.** Diffusion-weighted MR imaging sequences for evaluating tumors in the body*

| Technique | Breath-hold single-shot echo-planar (EPI) diffusion-weighted imaging (DWI) | Free-breathing multiple averaging single-shot EPI DWI | Whole-body DWI with background suppression |
|---|---|---|---|
| Field of view | 340–400 cm | 340–400 cm | 380–400 cm |
| Matrix size | 112×256 | 112×256 | 160×256 |
| Repetition time | 2500 | 3900 | >3500 ms |
| Echo time | 56–68 ms | 78 | 72 ms |
| Fat suppression | SPAIR | SPAIR/STIR | STIR |
| EPI factor | 65 | 59 | 47 |
| Parallel imaging factor | 2 | 2 | 2 |
| NSA | Single-shot | 5 | 6 |
| Section thickness | 7 mm contiguous | 5 mm | 4 mm/1 mm overlap |
| Directions of motion-probing gradients | Phase, frequency, and slice | Phase, frequency, and slice | Phase, frequency, and slice |
| b-factors (s/mm²) | usually 3 b-values (e.g., 0, 100, 500 s/mm²) | allows multiple b-values (e.g., 0, 50, 100, 250, 500, 750 s/mm²) | 0 and 1000 s/mm² |

* Imaging protocols as implemented on a Philip's 1.5T magnetic resonance imaging system
• STIR = Short-tau inversion recovery
• SPAIR = Spectral selected attenuated inversion recovery

tage of this technique is the number of b-values that can be accommodated within a single breath-hold, which may have bearing on the accuracy of ADC determination.

*Free-breathing multiple-averaging DWI.* The principle advantages of free-breathing multiple-averaging DWI are that signal averaging allows use of multiple b-values and thin slice partitions (e.g. 4 to 5 mm) and the technique yields images with high signal-to-noise. These images can be qualitatively assessed using multi-planar reconstruction (MPR) or maximum intensity projection (MIP) (Fig. 1).[7] In addition, DWI or ADC maps may be effectively laid over morphological information to produce fusion images that combine diffusion-weighted functional information with anatomical details (Fig. 1). Using multiple b-values also enables evaluation of the ADC of lesions. Thus, free-breathing multiple averaging DWI appears to be a versatile technique that allows good use of DWI images for both qualitative and quantitative analysis.

However, ADC calculation using this technique may be less optimal in characterizing smaller lesions or in reporting lesion heterogeneity because of volume averaging. So, there is considerable interest in combining such sequences with respiratory[8,9] and cardiac triggering techniques to improve image registration and ADC assessment. Not surprisingly, it has been shown that compared with free-breathing acquisition, the use of respiratory triggering in the liver lead to better contrast-to-noise ratio and a decrease in the scattering of ADC values.[8] However, implementing such a scheme in clinical imaging is challenging because it may further increase the already noticeable scan time of 4 to 6 min for each acquisition. Novel techniques that enable more efficient gains in signal acquisition during respiratory gating are being investigated and developed.

*Diffusion-weighted whole-body imaging with background body signal suppression (DWIBS).* DWIBS was conceived primarily as a method to visualize tumors in the body by their restricted water mobility. Because these images are usually evaluated qualitatively, only b-values of 0 and 1000 s/mm$^2$ are employed. Fat suppression and high b-value are used to maximize background suppression. Free-breathing multiple averaging DWI is repeated at contiguous imaging stations. The images are processed by MIP, composed together and displayed using an inverted gray scale.[7] The dataset can also be visualized in 3D using MPR and volume rendered (VR) displays (Fig. 2).

Signals from normal tissue, such as blood vessels, fat, muscle and bowel are usually suppressed, whereas other normal structures, such as the spleen, prostate, testes, ovaries, endometrium, and spinal cord, remain visible.[7] DWIBS detects not only tumor (i.e., restricted diffusion) but also hyperviscous fluids (i.e., nonrestricted diffusion with hyperviscosity), such as abscesses. The technique appears promising for detecting tumors of small volume in the lymph nodes, peritoneum, and other sites of occult disease.[7] It can also be used to visualize peripheral nerves as diffusion-weighted MR neurography (Fig. 3).[10]

DWIBS can be obtained using a sophisticated whole-body coil array system, like the total imaging matrix system (TIM, Siemens Medical Solutions, Malvern, Pennsylvania) or other commercially available long coil arrays. However, such imaging can also be achieved using just a single coil array. To do this, the patient lies on a table extension elevated from the MR table-top at the 2 ends by spacers. A 4-cm gap between the table extension and the MR table-top allows the posterior coil elements to be placed under the patient. Placing the posterior coil in this gap enables movement of its element freely to another imaging station without moving the patient or altering the referenced scan position. In this way, images acquired at different imaging stations can be composed to yield a whole-body image (Fig. 4).

DWIBS shares many of the advantages of free-breathing multiple averaging DWI, such as thin image partitions and good signal-to-noise. Its main disadvantage is the relatively long image acquisition time required to evaluate the entire body.

## Optimization of DWI in the Body

The image contrast at DWI relies on intrinsic differences in the water diffusion between tissues. To maximize this contrast to detect and characterize lesions, scanning parameters must be chosen that optimize signal and contrast-to-noise between the tumor and surrounding tissues and that minimize artifacts and other effects that may modify or confound the native diffusion-weighted contrast. Appreciation of these factors will help the radiologist make informed decisions at clinical scanning.

*Fat suppression.* Fat suppression is routinely employed to increase the dynamic range of the DWI images and reduce the chemical shift-induced ghosting that is prevalent in EPI. When performing DWI over a large area of the body, an inversion-recovery (e.g., STIR) approach is preferred because it is likely to produce more uniform fat suppression and is the method adopted for DWIBS. However,